

Synergistic polarization and oxygen vacancies engineering for enhancing photocatalytic NO removal over Bi₄Ti₃O₁₂ nanowires

Qiuhui Zhu^{a,b}, Yu Wang^{a,c}, Junjun Wang^{a,c}, Jianmin Luo^d, Jingsan Xu^e, Chuanyi Wang^{a,f,*}

^a School of Environmental Science and Engineering, Shaanxi University of Science and Technology, Xi'an 710021, China

^b Fujian Provincial Key Laboratory of Eco-Industrial Green Technology, College of Ecology and Resources Engineering, Wuyi University, Wuyishan 354300, China

^c School of Chemistry and Chemical Engineering, Shihezi University, Shihezi 832003, China

^d School of Chemistry and Civil Engineering, Shaoguan University, Shaoguan 512005, China

^e School of Chemistry and Physics & Centre for Materials Science, Queensland University of Technology, Brisbane, QLD 4000, Australia

^f Jiangxi Key Laboratory of Flexible Electronics, Flexible Electronics Innovation Institute, Jiangxi Science and Technology Normal University, Nanchang 330013, China

ARTICLE INFO

Keywords:

Oxygen vacancies
Polarization
Oriented growth
Photocatalytic NO removal
Bi₄Ti₃O₁₂ nanowires

ABSTRACT

Enhanced polarization emerges as a potent strategy for further enhancing the photocatalytic performance of a photocatalyst. Considering the anisotropy of ferroelectric polarization and the improvement of polarization by defects, [010] preferred growth Bi₄Ti₃O₁₂ nanowires with oxygen vacancies were prepared via a hydrothermal method. Bi₄Ti₃O₁₂ nanowires exhibited a photocatalytic NO removal efficiency of up to 67.5% under visible light irradiation ($\lambda > 420$ nm), which is much higher than that of its counterpart, Bi₄Ti₃O₁₂ (3%). Structural characterizations and theoretical calculations support that, the engineering of oxygen vacancies in Bi₄Ti₃O₁₂ can enhance the polarization in the [010] and [100] directions, and gradually shifted the polarization dominant direction of Bi₄Ti₃O₁₂ from [100] to [010]. Overall, the improved polarization and generated oxygen vacancies enhanced the photocatalytic NO removal performance of Bi₄Ti₃O₁₂ nanowires. This work elucidates the significance of rational engineering oxygen vacancy-based microstructures and utilizing the polarization to amplify the photocatalytic performance.

1. Introduction

The photocatalytic conversion of NO_x is an effective method for treating low concentrations of NO_x in the air. However, the recombination of photo-generated carriers limits the utilization efficiency of the photo-generated electrons and holes. Therefore, promoting the separation and migration of photo-generated carriers is an important method to improve photocatalytic efficiency [1]. Bismuth-based composite oxides have been widely used as efficient photocatalytic materials in environmental remediation and energy conversion [2]. In terms of the composition of the electronic structure, the involvement of Bi 6p and Bi 6s orbitals in bismuth-based composite oxides contributes to reducing the band gap and expanding their light absorption range. At the same time, the hybridization of O 2p and Bi 6s orbitals results in a discrete character of the valence band, which helps facilitate the migration of photo-generated holes and improve the utilization efficiency of photo-generated electrons and holes, thus enhancing photocatalytic efficiency [3]. Aurivillius phase bismuth-based composite oxides are

composed of perovskite-like layers (A_{m-1}B_mO_{3 m+1})²⁻ and (Bi₂O₂)²⁺ layers, where m represents the alternating layers along the c-axis. Their excellent ferroelectric polarization characteristics enable directed movement of free charges within the photocatalytic material, resulting in the generation of C⁺ and C⁻ surfaces [4]. Furthermore, in order to maintain electrical neutrality on the surface of the photocatalytic material, the ferroelectric polarization allows the adsorption of external charged molecules or ions through the shielding effect of the ferroelectric material to achieve charge balance. Therefore, during the photocatalytic process, ferroelectric polarization not only promotes the separation and migration of photo-generated carriers but also improves the adsorption of target molecules on the surface of the photocatalytic material [5].

As shown in Fig. 1b, Bi₄Ti₃O₁₂ (m=3) consists of perovskite-like layers (Bi₂Ti₃O₁₀)²⁻ and (Bi₂O₂)²⁺ [7], exhibiting good visible light absorption and ferroelectric polarization characteristics. For Bi₄Ti₃O₁₂, below the Curie temperature, it adopts an orthorhombic structure with lattice constants a = 5.448 Å, b = 5.411 Å, c = 32.83 Å. The dipole

* Corresponding author at: School of Environmental Science and Engineering, Shaanxi University of Science and Technology, Xi'an 710021, China.

E-mail address: wangchuanyi@sust.edu.cn (C. Wang).

<https://doi.org/10.1016/j.apcatb.2024.123734>

Received 4 December 2023; Received in revised form 9 January 2024; Accepted 12 January 2024

Available online 15 January 2024

0926-3373/© 2024 Elsevier B.V. All rights reserved.

moment generated by the non-coincidence of positive and negative charge centers within the unit cell results in the spontaneous polarization of $\text{Bi}_4\text{Ti}_3\text{O}_{12}$ [8]. Additionally, due to the insulating nature of the $(\text{Bi}_2\text{O}_2)^{2+}$ layer, it acts as a shield, and the polarization direction is usually parallel to the $(\text{Bi}_2\text{O}_2)^{2+}$ layer. Amritendu et al. [6] found through first-principles theoretical calculations that the ferroelectric polarization in $\text{Bi}_4\text{Ti}_3\text{O}_{12}$ is closely related to the ionic polarizability. As shown in Figs. 1a and 1b, the ionic polarizability of $\text{Bi}_4\text{Ti}_3\text{O}_{12}$ mainly originates from Ti^{4+} and O^{2-} , while Bi 2 and O 2 in the $(\text{Bi}_2\text{O}_2)^{2+}$ layer contribute little to the polarizability. Therefore, the ferroelectric polarization strength of $\text{Bi}_4\text{Ti}_3\text{O}_{12}$ is determined by Ti^{4+} and O^{2-} in the Ti-O octahedra. Furthermore, the direction of ferroelectric polarization forms an angle of 7.49° with the a-axis in the a-c plane and an angle of 21.94° with the b-axis in the a-b plane. The polarization strength of $\text{Bi}_4\text{Ti}_3\text{O}_{12}$ is mainly concentrated in the a-b plane and primarily along the a-axis. Dong et al. [9] calculated the contribution of each ion to the ferroelectric polarization of $\text{Bi}_4\text{Ti}_3\text{O}_{12}$ using formula (1):

$$P_s = \sum_i \frac{m_i \times \Delta x_i Q_i e}{V} \quad (1)$$

where m_i represents site multiplicity, Δx_i is the ion displacement, $Q_i e$ is the ion charge, and V is the cell volume. Subsequently, the polarization intensity vectors induced by each ion were summed, resulting in a theoretical polarization strength of $23.2 \mu\text{C}\cdot\text{cm}^{-2}$ for $\text{Bi}_4\text{Ti}_3\text{O}_{12}$ (Fig. S1).

The polarization of $\text{Bi}_4\text{Ti}_3\text{O}_{12}$ exhibits significant anisotropy in the a-b plane. Considering the origin and direction of polarization in $\text{Bi}_4\text{Ti}_3\text{O}_{12}$, if it is possible to orient the growth of $\text{Bi}_4\text{Ti}_3\text{O}_{12}$ along the a-axis and increase the number of Ti-O octahedra in the a-axis direction, it can improve the polarization strength along the a-axis of $\text{Bi}_4\text{Ti}_3\text{O}_{12}$. Furthermore, Alexandrov et al. [10] studied the influence of intrinsic defects on the ferroelectric polarization of SrTiO_3 using density functional theory and geometric phase analysis. The study found that line defects such as $\text{Ti}_{\text{Sr}}^{\bullet\bullet}$ and $\text{Sr}_{\text{Ti}}^{\bullet\bullet}$ enhanced the ferroelectric polarization strength of SrTiO_3 . Additionally, Frankel and Schottky defects also improved the spontaneous polarization of SrTiO_3 . In our previous work [11], we found that oxygen vacancies formed in the TiO_6 octahedra of $\text{SrBi}_4\text{Ti}_4\text{O}_{15}$ not only contributed to enhancing the spontaneous polarization strength of $\text{SrBi}_4\text{Ti}_4\text{O}_{15}$ in the [110] direction, promoting the separation of photo-generated charge carriers, but also broadened the photo responsive range and improved the photocatalytic performance for decomposing tetracycline.

Here, $\text{Bi}_4\text{Ti}_3\text{O}_{12}$ nanorods (BT-R) with preferential growth in the [010] crystal direction was prepared by hydrothermal method, and the addition of ethylene glycol promoted the growth of $\text{Bi}_4\text{Ti}_3\text{O}_{12}$ in the [010] crystal direction, resulting in the formation of oxygen vacancy modified $\text{Bi}_4\text{Ti}_3\text{O}_{12}$ nanowires (BT-L). BT-L is used for photocatalytic

conversion of ppb level NO_x under visible light ($\lambda > 420 \text{ nm}$) has a conversion efficiency of 67.5%. On the one hand, it is due to the increase in the number of Ti-O octahedra in the polarization direction of BT-L grown in the [010] crystal direction, which improves ferroelectric polarization, promotes the separation and migration of photo generated carriers, and the formation of oxygen vacancies increases the distortion rate of Ti-O octahedra, further increasing the polarization intensity in the [010] direction; On the other hand, the introduction of oxygen vacancies broadens the light response range and promotes the adsorption of target molecules on the BT-L surface. Subsequently, combined with DFT theoretical calculations, the influence of oxygen vacancies on $\text{Bi}_4\text{Ti}_3\text{O}_{12}$ in the [010] and [100] directions were revealed. The results showed that the polarization intensity of $\text{Bi}_4\text{Ti}_3\text{O}_{12}$ was mainly concentrated in the [010] direction and positively correlated with the concentration of oxygen vacancies.

2. Experimental sections

2.1. Chemical reagents

The chemical reagents used in this experiment have not undergone secondary purification treatment.

2.2. Preparation of photocatalysts

The preparation of $\text{Bi}_4\text{Ti}_3\text{O}_{12}$ was carried out by solid-state synthesis method. Firstly, Bi_2O_3 and TiO_2 (P25) with a molar ratio of 2:3 was accurately weighed in an agate mortar. Then, 10 mL of ethanol was added to the agate mortar to form a slurry. After grinding for 1 h, the agate mortar was placed in an oven and dried at 60°C for 1 h. After cooling to room temperature, the agate mortar was taken out and the mixture of the precursor was scraped off. After grinding for 10 min, fine particles were obtained. The obtained sample was placed in a corundum mortar and subjected to high-temperature calcination in a muffle furnace. The temperature was gradually increased to 850°C at a heating rate of $2^\circ\text{C}\cdot\text{min}^{-1}$ and maintained for 10 h. After prepared procedure was completed, the corundum crucible was cooled to room temperature, and after grinding for 10 min, a uniform solid powder was obtained, which was named as BT.

BT-L was prepared by a one-step hydrothermal method. 0.399 g of $\text{Bi}(\text{NO}_3)_3 \cdot 5 \text{H}_2\text{O}$ was dissolved in 25 mL of $2 \text{ mol}\cdot\text{L}^{-1}$ NaOH solution with stirring continuously for 30 min, labeled as suspension A. Then, 0.28 g of $\text{Ti}(\text{OC}_4\text{H}_9)_4$ was slowly added into suspension A, labeled as suspension B. After stirring at room temperature for 30 min, 0.455 g of $\text{C}_6\text{H}_{14}\text{O}_6$, 0.3 g of PVP, and 2 g of ethylene glycol were added into suspension B with stirring for 30 min. Meanwhile, the pH of solvent was adjusted to 12 using HNO_3 and NaOH. Subsequently, the suspension was

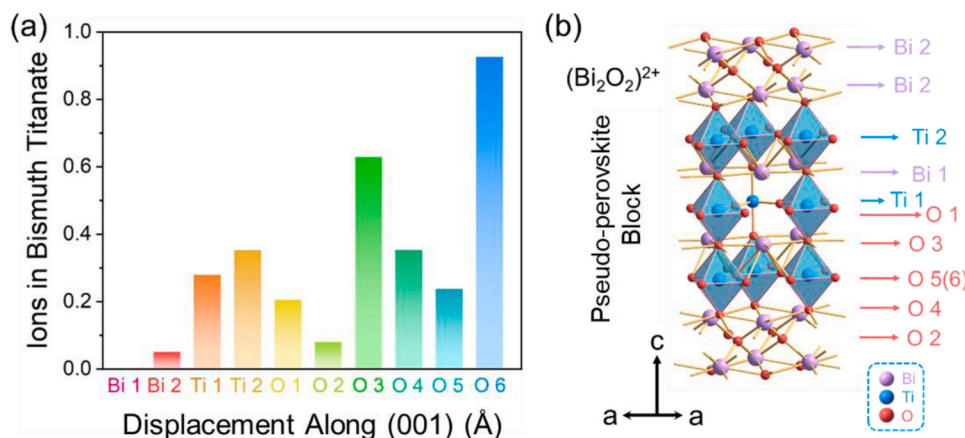


Fig. 1. (a) Displacement vectors of individual ions along a axis [6] and (b) schematic diagram of crystal structure of $\text{Bi}_4\text{Ti}_3\text{O}_{12}$.

transferred to a 50 mL Teflon-sealed autoclave and maintained it in an oven for 24 h at 170 °C. After the program was completed, the autoclave was to cool naturally to room temperature. The obtained suspension was then centrifuged and washed several times with deionized water and ethanol until the rinsing solution was neutral. Finally, the BT-L was dried in a 60 °C oven for 10 h. The preparation of BT-R and BT-LS was shown in SI.

2.3. Characterizations

Crystal phases of catalysts were performed using X-ray powder diffraction (XRD) with Cu K α radiation from a Rigaku Co. D/max2200PC instrument. The micromorphology of catalysts was carried out using a scanning electron microscope (SEM) and transmission electron microscopy (TEM) from FEI Verios 460 and JEM-2010, respectively. Photoluminescence spectra (excitation wavelength: 325 nm) and decay curves were measured using the Edinburgh FLSP 920 fluorescence spectrometer. X-ray photoelectron spectroscopy (XPS) with Al K α X-rays ($h\nu = 1486.6$ eV) radiation operating at 150 W (AXIS Supra, Kratos, UK) was used to examine the surface chemical composition and valence states with the C 1s peak (284.8 eV) serving as a calibration standard. Electron Paramagnetic Resonance (EPR) measurements were conducted using a Bruker E500 equipment, where the EPR signals of ROs were spin-trapped by 5,5-dimethyl-1-pyrroline N-oxide (DMPO). Superoxide radicals ($\bullet\text{O}_2^-$) and hydroxyl radicals ($\bullet\text{OH}$) were detected by dissolving the samples in DMPO aqueous solution and methanol solution, respectively. UV–vis diffuse reflectance spectra (DRS) of as-prepared samples in the 200–800 nm range were obtained by UV–vis diffuse spectrophotometer (UV-3700, Shimadzu, Japan) with 100% BaSO $_4$ as the reference.

2.4. Evaluation of photocatalytic performance

Using a 300 W xenon lamp (with a 420 nm cut-off filter) as simulated sunlight, the photocatalytic oxidation of ppb level NO through a continuous flow reactor was used to evaluate the photocatalytic performance of the prepared samples (Fig. S2). The mixture of NO and air flowed continuously (0.284 L·min $^{-1}$ controlled by a mass flow controller) on the surface of the prepared photocatalysts, the NO concentration was controlled at about 800 ppb, and the relative humidity in glass reactor was 5%. The concentrations of NO and NO $_2$ were monitored with a NO $_x$ analyzer (Model 42i, Thermal Fisher Scientific, USA). 50 mg of sample powder was dispersed in 10 mL of deionized water by sonication for 20 min to form a homogeneous suspension. And then, the suspension was transferred to a petri dish ($R = 3$ cm), which was vacuum-dried at 60 °C. Finally, the petri dish was placed into a glass reactor with a volume of 0.785 L ($R = 5$ cm, $L = 10$ cm) and a quartz lid. After reaching the adsorption-desorption equilibrium, the xenon lamp was turned on to start the photocatalytic reaction. The photocatalytic NO removal efficiency was calculated as follows: $\eta_{\text{NO}} = (1 - C/C_0) \times 100\%$, where C_0 and C represent the initial and real-time NO concentrations, respectively. The NO $_2$ yield is calculated according to the following formula: $\eta_{\text{NO}_2} = ([\text{NO}_2]_{\text{out}} - [\text{NO}_2]_{\text{in}})/(C_0 - C) \times 100\%$. $[\text{NO}_2]_{\text{out}}$ and $[\text{NO}_2]_{\text{in}}$ is the outlet and inlet concentration of NO $_2$, respectively. *In situ* DRIFTS experiments were used to explore the pathway of photocatalytic NO removal, and the detailed process can be found in the supporting information. Furthermore, the scheme of *in situ* DRIFTS is shown in Fig. S3.

2.5. DFT calculations

The Vienna ab initio package [12] is used to perform DFT calculations within the generalized gradient approximation using the Perdew–Burke–Ernzerh [13] of formulation. We have chosen the projected augmented wave potential [14] to describe the ion core and consider the valence electrons using a plane wave basis set with a kinetic energy

cutoff of 450 eV. Partial occupation of the Kohn-Sham orbitals was achieved using the Gaussian smear method with a width of 0.05 eV. Electron energies are considered self-consistent when the energy change is less than 10^{-4} eV. The geometry optimization is considered converged when the change in force is less than 0.05 eV Å $^{-1}$. The equilibrium structure of the unit cell is optimized using a $5 \times 2 \times 5$ Monkhorst–Pack k-point grid for Brillouin zone sampling.

3. Results and discussion

The XRD patterns of as-prepared samples were presented in Fig. 2a. The crystal structures of BT, BT-R, and BT-L are in good with the orthorhombic Bi $_4$ Ti $_3$ O $_{12}$ (JCPDS No.72–1019). In addition, the formation of the (117) peak in the X-ray diffraction pattern also conforms to the pattern observed in layered bismuth-based photocatalytic materials, which typically exhibit the strongest diffraction peak at $(112m+1)$ [15]. Therefore, the above results indicated the successful synthesis of the Bi $_4$ Ti $_3$ O $_{12}$ photocatalysts. The micro morphology of as-prepared samples was further explored by SEM, TEM, and AFM. As shown in Fig. 2b and S4a, Bi $_4$ Ti $_3$ O $_{12}$ prepared by a solid-phase synthesis exhibited irregular shapes, with an average diameter of around 1 μm . And then, hydrothermal method was employed to prepared BT-R with adding structure-inducing agents at pH = 11. As presented in SEM image of BT-R (Fig. 2c and S4b), the shape of nanorods is regular and the average length of BT-R to be 495 ± 0.1 nm with length distribution between 300–600 nm (Fig. 2d). In addition, the diameter of BT-R was around 35 nm determined by AFM (Fig. S5). As depicted in Fig. 2e, BT-R exhibited rod-shaped structures, consistent with SEM images, further confirming the formation of nanorods. The HRTEM image of BT-R (Fig. 2f) revealed a lattice spacing of 0.271 nm, which matched with (020) plane of orthorhombic Bi $_4$ Ti $_3$ O $_{12}$. The HRTEM results can confirm that Bi $_4$ Ti $_3$ O $_{12}$ nanorods grown along the [010] direction. Additionally, HRTEM image showed areas of low diffraction intensity and no lattice fringes in certain regions of the BT-R nanorods, which suggested the formation of defects leading to lattice disorder [16]. As shown in Fig. S4c, BT-R nanorods consisted of Bi, Ti, and O elements. The probably growth mechanism of BT-R was proposed. Mannitol in solution can adsorb on the terminating oxygen of the (Bi $_2$ O $_2$) $^{2+}$ layer, thus reducing the growth rate of BT-R in the [100] and [001] directions [17,18]. Additionally, H $^+$ exhibits specific adsorption on the (010) crystal plane, which can inhibit the growth rate of Bi $_4$ Ti $_3$ O $_{12}$ in the [010] direction. The presence of OH $^-$ weakens the interaction between H $^+$ and the terminating oxygen of the (010) crystal plane in alkaline conditions [19, 20], promoting the growth of Bi $_4$ Ti $_3$ O $_{12}$ along the [010] direction. Therefore, the precise pH and appropriate concentration of mannitol put forward the formation of rod-shaped Bi $_4$ Ti $_3$ O $_{12}$. Polyvinylpyrrolidone (PVP) acted as a stabilizer and dispersant during the formation process of the nanorods, resulting in a more uniform distribution of BT-R nanorods. SEM, TEM, and AFM images of BT-L (Figs. 2g and S6) indicated BT-L exhibited a wire-like shape with the average diameter of around 20 nm. According to HRTEM and SEAD results (Fig. 2h), the lattice spacing of BT-L was determined to be 0.271 nm consistent with BT-R, which also corresponded to (020) crystal face of orthorhombic Bi $_4$ Ti $_3$ O $_{12}$. Therefore, the hydroxyl-rich ethylene glycol can inhibit the growth rate of Bi $_4$ Ti $_3$ O $_{12}$ in the [100] and [001] directions, thus accelerating the epitaxial growth along [010] direction. Moreover, the lattice dislocation and disorder of BT-L indicated the generation of defects. And, BT-L also consisted of Bi, Ti, and O elements (Fig. 2i). Bi $_4$ Ti $_3$ O $_{12}$, as a typical ferroelectric photocatalytic material, derives its intrinsic polarization from the polarization of TiO $_6$ octahedra [21], which forms an internal electric field that can promote the directional migration of photo-generated charge carriers and thus improve photocatalytic efficiency [22]. In order to reveal the effect of intrinsic polarization on the internal charges of Bi $_4$ Ti $_3$ O $_{12}$, KPFM was employed to detect the surface potential of BT-R and BT-L, and to explain the role of ferroelectric polarization in charge separation [23]. Furthermore, the stacking of TiO $_6$

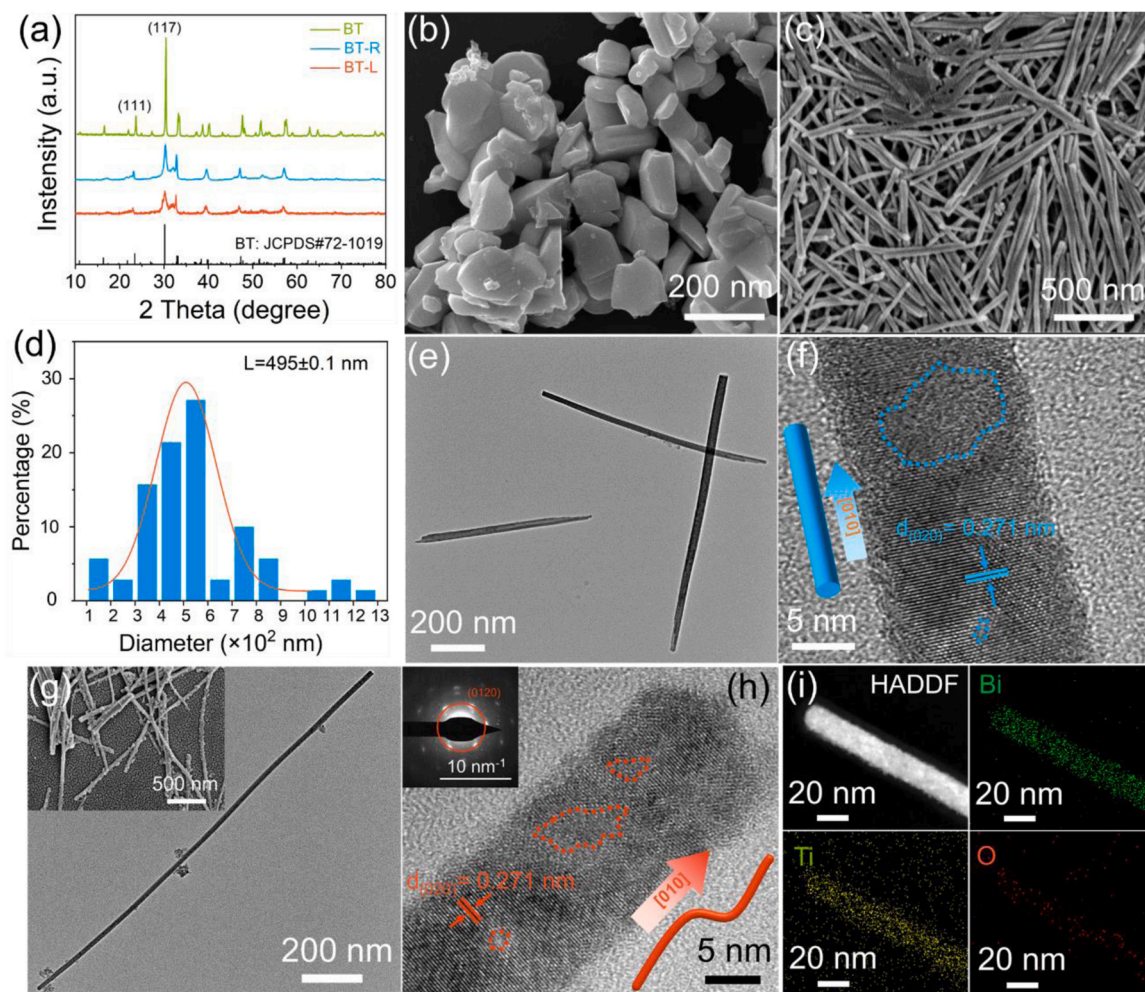


Fig. 2. (a) XRD patterns of BT, BT-R and BT-L, SEM images of (b) BT and (c) BT-R, (d) histogram of length distribution of BT-R, (e) TEM and (f) HRTEM of BT-R, (g) TEM of BT-L (inset: SEM image of BT-L), (h) HRTEM of BT-L (inset: the SAED pattern of BT-L) and (i) EDS mapping images of BT-L.

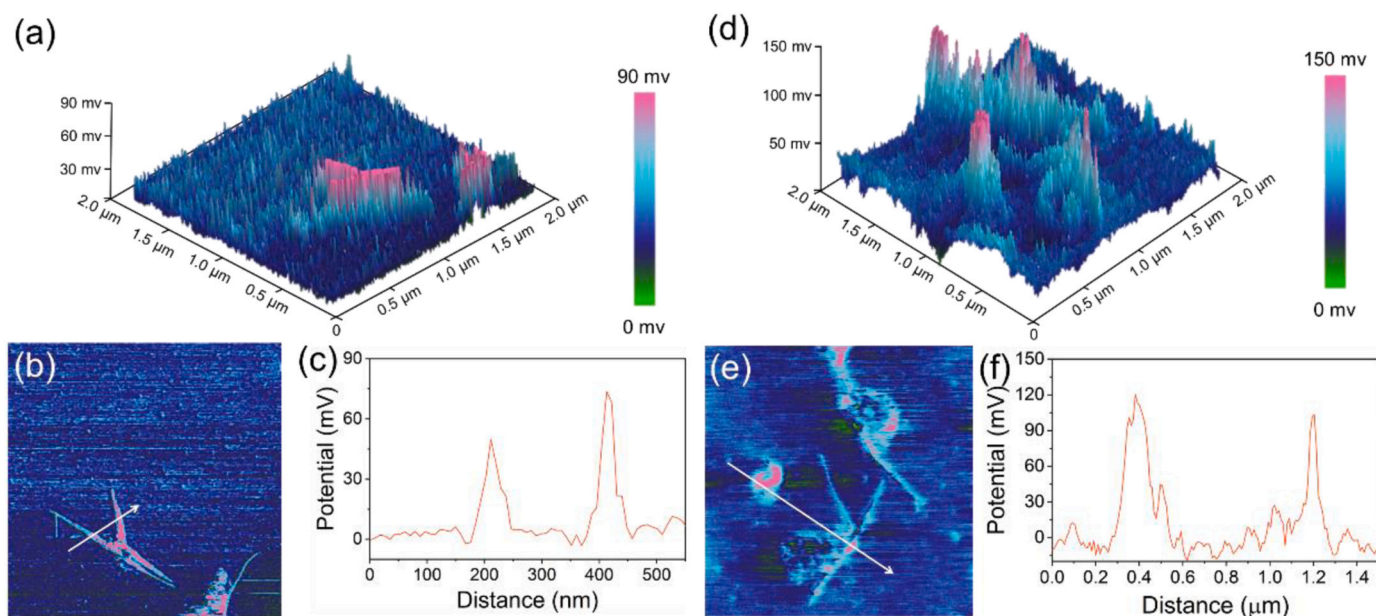


Fig. 3. Surface potential difference of BT-R and BT-L: (a, d) 3D and (b, e) 2D images and (c, f) corresponding surface potential curves.

octahedra in the polarization direction can also explain the improvement of ferroelectric polarization. As shown in Figs. 3a–3c, the surface potential of BT-R surface exhibited a significant potential difference of 70 mV at the straight line with an arrow. And, BT-L showed a potential difference of 120 mV, which was much larger than BT-R (Figs. 3d–3f). The above results suggested that BT-L may have the better ferroelectric performance compared to BT-R, which can effectively suppress the recombination of photocatalytic carriers.

Furthermore, the electric hysteresis loops for as-prepared samples were conducted to reveal the ferroelectric performance and the polarization electric field is mainly contributed by P_r after the corona poling. As illustrated in Fig. 4a, the values of P_r were found to be 0.41, 0.46 and $0.59 \mu\text{C}\cdot\text{cm}^{-2}$ for BT, BT-R and BT-L, respectively. The improved ferroelectric polarization may be attributed to the generation of oxygen vacancies and the directional growth of $\text{Bi}_4\text{Ti}_3\text{O}_{12}$ along the [010] direction. Combined with the results of KPFM, the enhanced surface potential was resulted from ferroelectric polarization. In order to elucidate the influence of microstructure of $\text{Bi}_4\text{Ti}_3\text{O}_{12}$ on the polarization, DFT calculations were employed to investigate the role of concentration oxygen vacancies and growth orientation on the improved ferroelectric polariton. The crystal structures of defect-free $\text{Bi}_4\text{Ti}_3\text{O}_{12}$ as well as $\text{Bi}_4\text{Ti}_3\text{O}_{12}$ with 5% and 10% oxygen vacancies concentrations were constructed and optimized. Furthermore, the effects of different oxygen vacancies concentrations along the [100] and [010] directions on the polarization intensity of $\text{Bi}_4\text{Ti}_3\text{O}_{12}$ were explored, respectively. By calculating the difference in the polarization rate of $\text{Bi}_4\text{Ti}_3\text{O}_{12}$ before and after defect construction using the formula 1, the magnitude of the polarization intensity can be obtained. As shown in Fig. 4b and Table S1, defect-free $\text{Bi}_4\text{Ti}_3\text{O}_{12}$ has polarization intensities of $7.17 \mu\text{C}\cdot\text{cm}^{-2}$, while $\text{Bi}_4\text{Ti}_3\text{O}_{12}$ with 5% and 10% oxygen vacancies concentrations have polarization intensities of $7.53 \mu\text{C}\cdot\text{cm}^{-2}$ and $8.32 \mu\text{C}\cdot\text{cm}^{-2}$, respectively. The polarization intensity of $\text{Bi}_4\text{Ti}_3\text{O}_{12}$ along the [100] direction have a slight increase with increasing oxygen vacancy concentration. Specifically, the polarization intensities of defect-free, 5% and 10% oxygen vacancies concentration of $\text{Bi}_4\text{Ti}_3\text{O}_{12}$ along the [010] direction are 3.43, 17.18, and $23.25 \mu\text{C}\cdot\text{cm}^{-2}$, respectively. The above results indicate a positive correlation between oxygen vacancies concentration and the polarization intensity of $\text{Bi}_4\text{Ti}_3\text{O}_{12}$. In addition, the impact of oxygen vacancies on polarization intensity is much greater along the [010] direction compared to the [100] direction. Furthermore, as the oxygen vacancy concentration increases, the predominant polarization direction of $\text{Bi}_4\text{Ti}_3\text{O}_{12}$ gradually transitions from [100] to [010] direction. Therefore, considering the crystal orientations of BT, BT-R, and BT-L (Fig. S7), the improved polarization may be attributed the generation of oxygen vacancies and the stacking of TiO_6 polyhedron in the polarization direction of [010].

XPS was employed to determine the chemical composition and states and the results implied the presence of Bi, Ti, and O in BT and BT-L

(Fig. S8 and Table S2). The high-resolution XPS spectra of Bi 4f, Ti 3d, and O 2p was further studied. As shown in Fig. 5a, the peaks centered at 485.6 and 451.1 eV are attributed to the Ti $2p_{1/2}$ and Ti $2p_{3/2}$, respectively, both of two peaks in BT-L show a slight shift to the lower binding energy compared to BT. The results indicated that the electron-donating sites formed by defects on the surface of BT-L, which can increase the electron cloud density of the outermost Ti^{4+} . The characteristic peaks of BT and BT-L at 156.1 and 161.4 eV corresponded to the Bi $4f_{5/2}$ and Bi $4f_{7/2}$ (Fig. 5b), and the peak positions have not significantly changed. For the O 1s spectrum of BT-L (Fig. 5c), three main peaks were observed at the binding energies of 526.7, 528.1, and 528.8 eV, corresponding to lattice oxygen, adsorbed oxygen species, and surface hydroxyl groups [24]. However, only two characteristic peaks at 526.6 and 527.6 eV for O 1s in BT were found. Additionally, the peak area corresponding to the adsorbed oxygen species and surface hydroxyl groups in BT-L was larger than that in BT, which was attributed to the presence of defects on the surface of BT-L [25]. And, the characteristic peaks of lattice oxygen and adsorbed oxygen species in BT have a shift towards higher binding energy. EPR was employed to detect the defects in BT, BT-R, and BT-L. As shown in Fig. 5d, BT-R and BT-L have symmetric EPR signals at $g = 2.003$ [26], which was ascribed to the single electrons captured by oxygen vacancies. Moreover, the signal intensity of BT-L was higher than BT-R.

The generation of OV in photocatalysts can expand the range of light response [27]. Therefore, the UV–vis DRS was conducted to evaluate the light absorption capability of as-prepared samples in the range of 200–1200 nm. As shown in Fig. 5e, the performance of visible light range followed the order: BT-L > BT-R > BT. Moreover, BT-R and BT-L show distinct Urbach tails, with BT-R tail extending up to 650 nm and BT-L tail extending up to 1150 nm, which was due to the generation of OVs in BT-R and BT-L. The band gap of samples was calculated by the Kubelka-Munk equation. As shown in Fig. 5f, the band gaps were ranked as follows: BT (2.91 eV) > BT-R (2.78 eV) > BT-L (2.77 eV). The UPS and XPS was conducted to reveal the influence of OVs on the band structure. The work functions of BT and BT-L was 4.61 and 4.37 eV (Fig. 6a), respectively, which was calculated by following equation: $\Phi = h\nu - E_{\text{cutoff}} + E_{\text{Fermi}}$ [28], where E_{cutoff} is the cutoff region, and the energy of the incident photons from the He I source is 21.22 eV, denoted as $h\nu$. Compared to BT, BT-R and BT-L have narrower bandgaps, which may be attributed to the generation of OVs. The conduction band of $\text{Bi}_4\text{Ti}_3\text{O}_{12}$ is mainly composed of Ti 3d, and the valence band is mainly composed of O 2p and Bi 6s [29]. Therefore, the formation of OVs in BT-R and BT-L can optimize the band structure of $\text{Bi}_4\text{Ti}_3\text{O}_{12}$ and generate intermediate energy levels, which can be determined as follows [30,31]:

$$\ln \alpha = h\nu/E_u + \ln \alpha_0 \quad (2)$$

where α is the absorbance, h is the Planck constant, ν is the frequency,

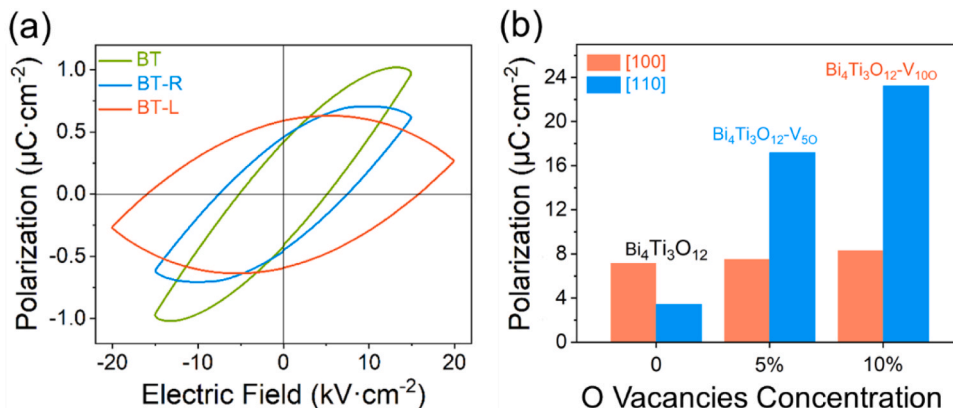


Fig. 4. (a) Electric hysteresis loop and (b) DFT calculated polarization of BT, BT-R and BT-L.

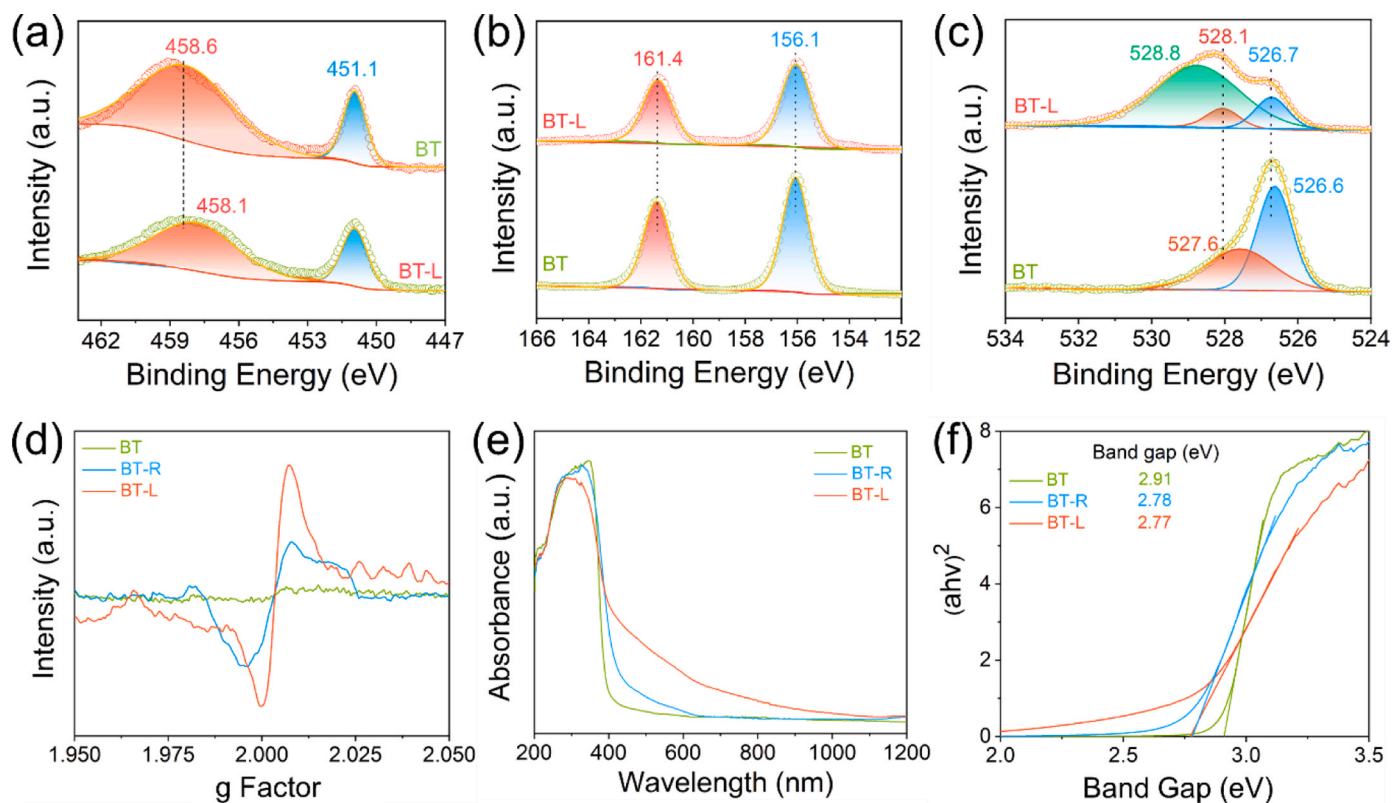


Fig. 5. High resolution XPS spectra of (a) Ti 2p, (b) Bi 4f and (c) O 1s, (d) EPR spectra of BT, BT-R and BT-L, (e) UV-vis DRS and (f) band gap of BT, BT-R and BT-L.

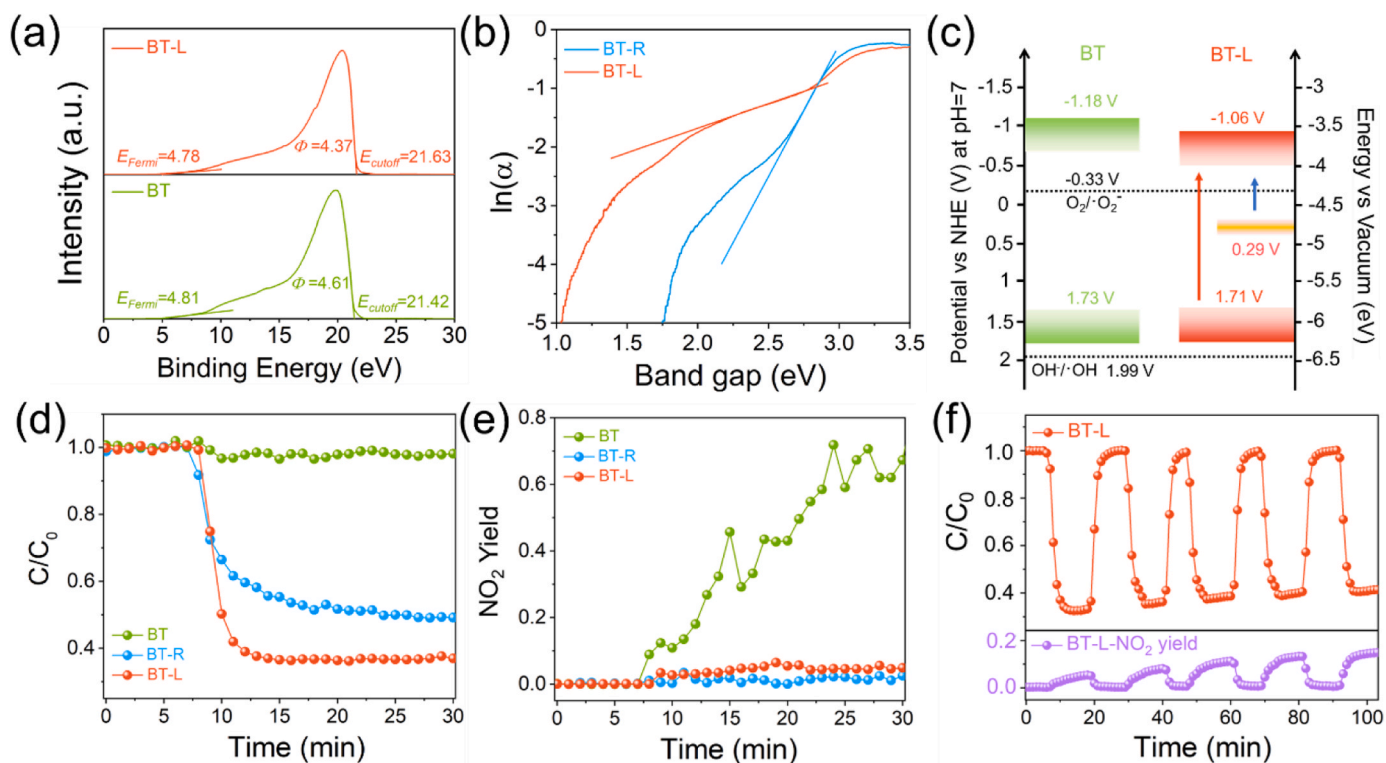


Fig. 6. (a) UPS of BT and BT-L, (b) the intermediate band gap of BT-R and BT-L, (c) schematic diagram of band gap of BT and BT-L (d) Photocatalytic NO removal efficiencies and (e) NO_2 yields of BT, BT-R and BT-L, and (f) five cycling runs for photocatalytic removal NO and corresponding NO_2 yield over BT-L.

and α_0 is the Urbach constant. As shown in Fig. 6b, the intermediate band gap of BT-R and BT-L were 0.35 eV and 1.21 eV, respectively. Furthermore, the energy width between valance band maximum and Fermi level can be determined by VB-XPS, and BT and BT-L of that were 1.56 and 1.78 eV, respectively (Fig. S9). Therefore, the valance band of BT and BT-L were 6.17 and 6.15 eV vs vacuum level (1.73 and 1.71 V vs NHE), respectively (Fig. 6c). The conduction band were estimated to be -1.18 and -1.06 V.

The photocatalytic performance of as-prepared samples was evaluated for converting of ppb-level NO in a flow phase under visible light irradiation ($\lambda > 420$ nm). As shown in Fig. 6d, BT-L exhibited optimized photochemical conversion activity for NO (67%) compared to BT-R (59%) and BT (3%). The performance of photocatalytic NO removal using BT-L is better compared to representative reports previously (detailed comparison can be found in Table S3). Moreover, the results of real-time monitoring of NO_2 during the photocatalytic process in BT, BT-R, and BT-L revealed that BT-L not only demonstrated outstanding performance in NO conversion but also exhibited low NO_2 generation (Fig. 6e), which may be attributed to the formation of oxygen vacancies that can facilitate NO adsorption and promote the generation of reactive oxygen species. Furthermore, five cycles evaluation for photocatalytic conversion of NO process was employed to investigate the stability of BT-L, the result showed a decrease in the performance from 67% to 61% for BT-L (Fig. 6f). In order to further assess the photocatalytic NO removal performance of BT, BT-R and BT-L, the DeNO_x index was utilized, considering the higher toxicity of NO_2 compared to NO. The detailed information regarding the DeNO_x index can be found in the Supporting Information. As depicted in Fig. S10, the DeNO_x index values of BT, BT-R and BT-L were -0.04 , 0.43 and 0.61 , respectively. The results indicated that BT-L was suitable for the photocatalytic NO removal. Meanwhile, the concentration of NO_2 gradually increased with prolonged reaction time. The result could be due to the accumulation of NO_3^- , NO_2^- , and other oxidation products adsorbed on the surface of BT over time, thereby reducing its durability [32,33]. In addition, it is

evident that the crystal structure of BT-L was negligibly altered after five cycles of photocatalytic NO removal (Fig. S11).

To reveal the influence of oxygen vacancies on the optical properties and photocatalytic performance for NO removal in BT-L, BT-L was recalcined in the O_2 -rich atmosphere to removal oxygen vacancies. As shown in Fig. 7a, the diffraction peak position of the calcined BT-L (BT-LS) did not change significantly, but the diffraction peak intensity increased, indicating better crystallinity of the BT-LS after calcination, possibly due to the re-filling of O atoms into the disordered surface. In addition, it was found by EPR characterization that the concentration of oxygen vacancies in BT-LS was significantly lower than that in BT-L (Fig. 7b). Furthermore, it can be seen from the results of DRS spectrum (Fig. 7c) that the Urbach tail of BT-LS disappeared after calcination, possibly due to the decrease in concentration of oxygen vacancies of BT-LS. As shown in Fig. 7d, the bandgap of BT-LS increased from 2.78 eV to 2.82 eV when calculated by the Kubelka-Munk formula, further indicating the optimizing effect of oxygen vacancies on the bandgap. Subsequently, the photocatalytic performance of BT-LS in converting NO was evaluated (Figs. 7e and 7f). Compared to BT-L, the photocatalytic efficiency of BT-LS decreased from 67% to 28%, and the production of NO_2 increased significantly. The above characterization and performance testing results further demonstrate the role of oxygen vacancies in BT-L in the bandgap and photocatalytic conversion of NO.

The recombination rate between photo-generated electrons and holes can be determined by fluorescence intensity, which reflects the utilization efficiency of photo-generated electrons. As shown in Fig. 8a, both BT and BT-L exhibit distinct fluorescence emission peaks under the excitation wavelength at 325 nm. The intensity of the peak over BT-L was sharp decreased compared to BT, indicating a lower recombination rate of photo-generated electrons and holes in BT-L. Furthermore, the time-resolved photo-luminescence (TRPL) spectroscopy was employed to investigate the lifetime of photogenerated electrons. It could be found in Fig. 8b that the average lifetime of BT-L was 4.36 ns, which was higher than that in BT (3.27 ns). The lower recombination

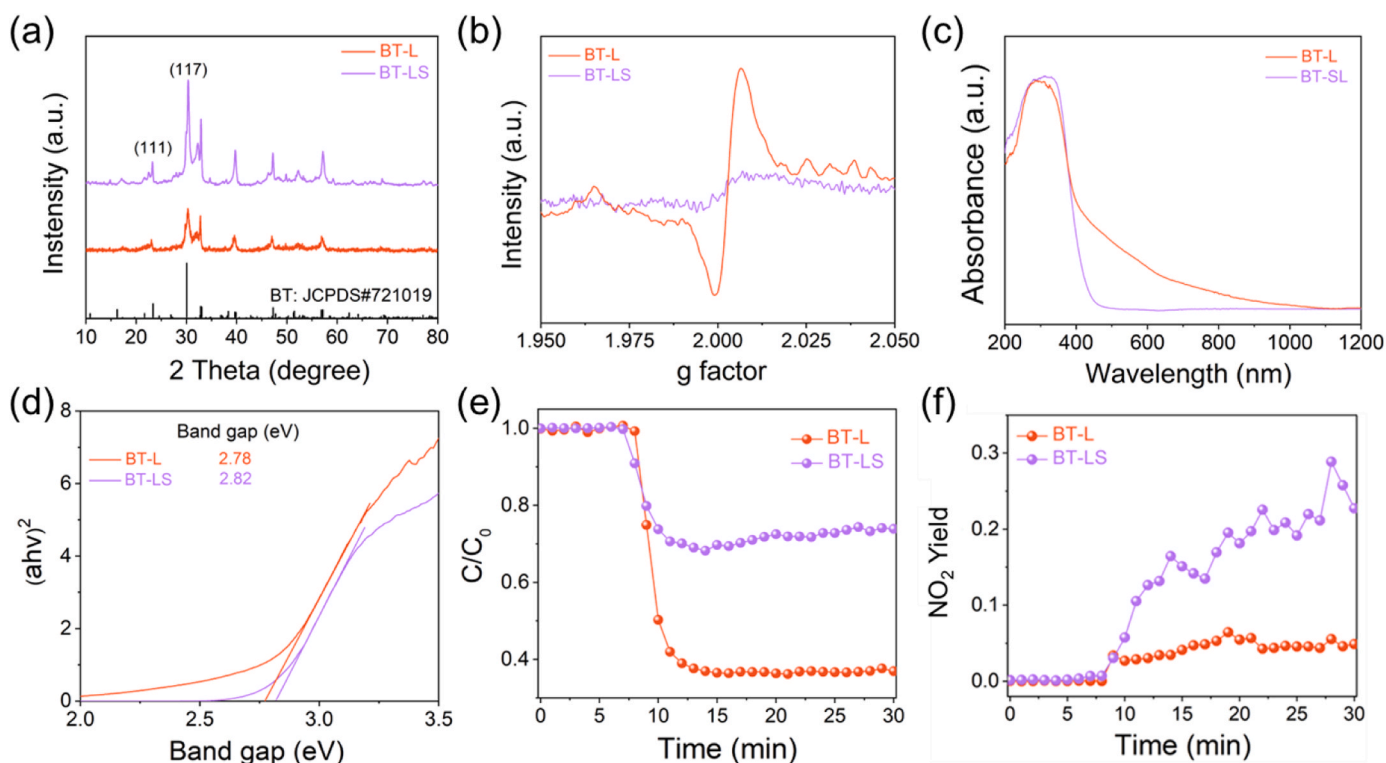


Fig. 7. (a) XRD, (b) EPR, (c) DRS, (d) band gap of BT-L before and after calcination, and (e) photocatalytic NO removal efficiency and (f) NO_2 yield of BT-L before and after calcination.

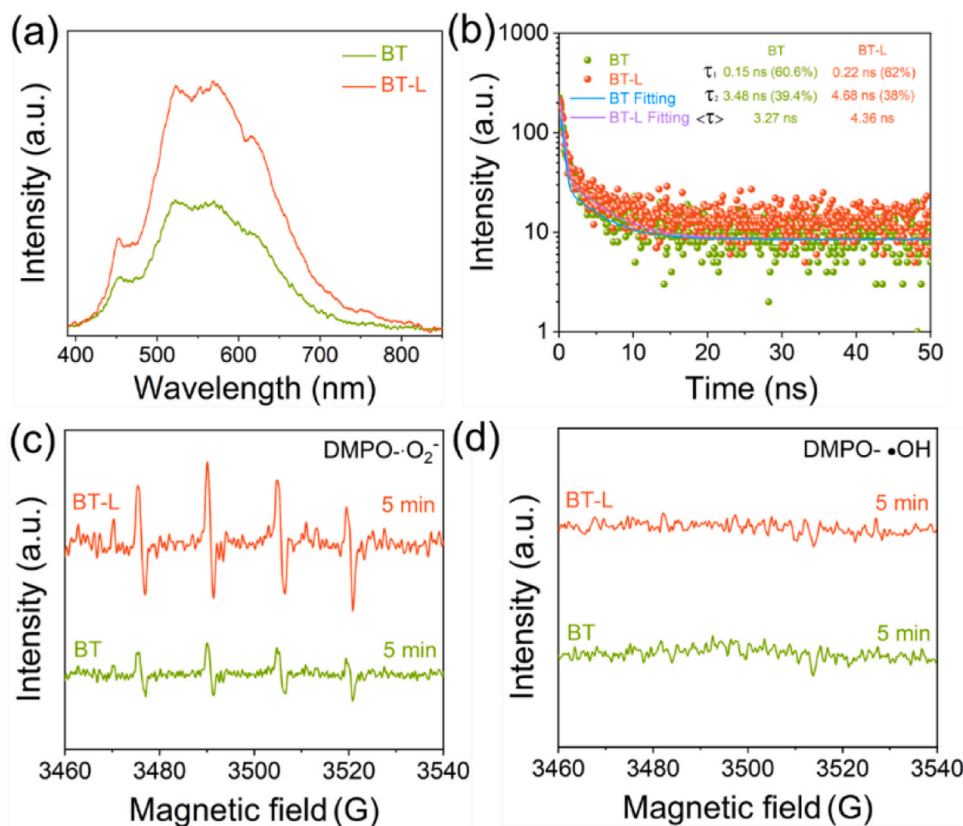
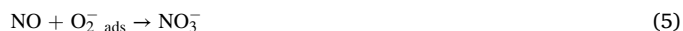
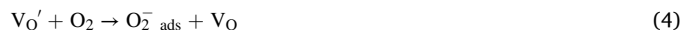


Fig. 8. (a) PL spectra, (b) the ns-level time-resolved fluorescence spectrum of BT and BT-L, EPR signals of (c) $\text{DMPO} \cdot \text{O}_2^-$ and (d) $\text{OH} \cdot$ for BT and BT-L under visible light.

probability and longer lifetime of photogenerated carriers in BT-L, as opposed to BT, can be attributed to two main factors. 1) The improved ferroelectric polarization intensity in BT-L accelerates the directed migration and separation of photo-generated charge carriers and increases the retention time of photo-generated electrons. 2) The intermediate energy levels induced by oxygen vacancies in BT-L can also inhibit the recombination of photoexcited electrons and holes. Overall, the combination of improved ferroelectric polarization and generated oxygen vacancies in BT-L promotes the directed migration and separation of photogenerated carriers, thereby resulting in a lower recombination probability and longer carrier lifetime. The main reactive oxygen species (ROS) are closely related to the photocatalytic removal efficiency of NO and the generation of toxic NO_2 . EPR was employed to detect the signals of ROS over BT and BT-L under illumination. As shown in Fig. 8c, both BT and BT-L exhibited EPR signals of $\text{O}_2^- \cdot$ with a peak intensity ratio of 1:1:1:1 after 5 min of illumination ($\lambda > 420$ nm). And, the intensity of $\text{O}_2^- \cdot$ EPR signal in BT-L was higher than in BT, suggesting that BT-L generated a higher concentration of $\text{O}_2^- \cdot$ within 5 min of illumination. However, there was no EPR characteristic signal representing $\text{OH} \cdot$, indicating that neither BT nor BT-L can generate $\text{OH} \cdot$ under visible light illumination (Fig. 8d). Furthermore, photocatalytic capture experiments were employed to further illustrate the role of active species (e^- , h^+ , $\text{O}_2^- \cdot$, and $\text{OH} \cdot$) in the BT-L photocatalytic conversion of NO. $\text{K}_2\text{Cr}_2\text{O}_7$, KI, p-benzoquinone (PBQ), and isopropanol (IPA) were used to capture e^- , h^+ , $\text{O}_2^- \cdot$, and $\text{OH} \cdot$, respectively. As shown in Fig. S12, the photocatalytic activity of BT-L was significantly inhibited after adding $\text{K}_2\text{Cr}_2\text{O}_7$, KI, and PBQ. The addition of IPA to capture $\text{OH} \cdot$ did not lead to a decrease in BT-L photocatalytic activity, indicating that there was no $\text{OH} \cdot$ produced in the system, which is consistent with the EPR results. The capture experiment results showed that e^- , h^+ , and $\text{O}_2^- \cdot$ play the main role in the BT-L photocatalytic conversion of NO.

In situ DRIFTS was employed to monitor the dynamic changes of

surface species during NO adsorption and photocatalytic oxidation processes in real-time, thereby further exploring the pathway and reaction mechanism of photocatalytic conversion of NO over BT-L. As shown in Fig. S13, during the dark adsorption process, with the continuous introduction of a mixture of NO and O_2 , a characteristic peak attributed to NO appeared at 1052 cm^{-1} , and the intensity of the characteristic peak gradually increased with time. When the concentration of NO is at the ppb level, the reaction rate between NO and O_2 is very slow. However, during *in situ* DRIFTS testing, the reaction rate of between NO at a concentration of 50 ppm and O_2 increased ($2\text{NO} + \text{O}_2 \rightarrow 2\text{NO}_2$), thus the characteristic peak at 2966 cm^{-1} belonged to NO_2 . The characteristic peak that appeared at 1095 cm^{-1} was attributed to NOH, which resulted from the NO and H bond generated by hydrolysis dissociation. In addition, the characteristic peak appearing at 1645 cm^{-1} was assigned to $m\text{-NO}_3^-$, which may be due to the reaction between oxygen vacancies confined e^- with O_2 to form O_{ads}^- , which in turn forms NO_3^- with NO (chemical equations 3–5).



As shown in Fig. 9, various characteristic peaks attributed to NO derivatives appeared on the surface of BT-L under illumination. Specifically, the peak at 1281 cm^{-1} was attributed to bidentate nitrate ($bi\text{-NO}_3^-$). And, the bridging nitrate ($br\text{-NO}_3^-$) are observed at 1070 cm^{-1} and $2800\text{--}2950 \text{ cm}^{-1}$. Subsequently, the peaks at 1169 cm^{-1} and $1550\text{--}1620 \text{ cm}^{-1}$ appeared, which were attributed to chelating nitrate ($c\text{-NO}_2^-$) and monodentate nitrate ($m\text{-NO}_3^-$), respectively. The assignments of observed characteristic peaks during photocatalytic removal NO over BT-L were shown in Table 1. As mentioned above, the main intermediates and products of photocatalytic NO removal over BT-L are

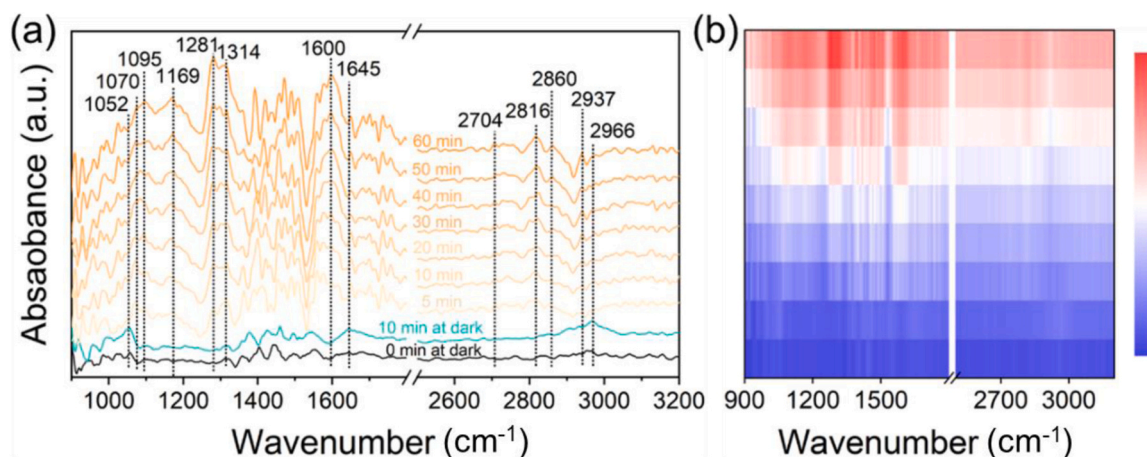


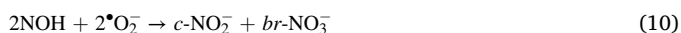
Fig. 9. (a) *In situ* DRIFTS spectra of BT-L for adsorption and photocatalytic removal of NO, and (b) corresponding heat map.

Table 1

Assignments of the IR bands observed during photocatalytic removal NO over BT-L under irradiation.

Wavenumber (cm ⁻¹)	Assignment	References
1052	NO	[34]
1070	Bridging nitrate	[35]
1095	NOH	[36]
1169	Chelated nitrite	[37]
1281	Bidentate nitrate	[38]
1314	Monodentate nitrate	[36]
1550-1620	Bidentate nitrate	[37]
1645	NO	[34]
2800-2950	Bridging nitrate	[35]
2966	NO ₂	[39]

bi-NO₃⁻ at 1281 cm⁻¹ and *m*-NO₃⁻ at 1314 cm⁻¹. Based on the *in situ* DRIFTS results, the reaction pathway for photocatalytic conversion of NO over BT-L was as follows:



Overall, the oxygen vacancies in BT-L not only broadened the light response range, but also improved the intrinsic polarization. Furthermore, the ferroelectric polarization in BT-L can facilitate the migration of photogenerated charges from the bulk to surface through band bending, but also facilitate the directional separation of photogenerated electrons and holes. Photogenerated charge carriers migrating to the surface undergo redox reactions with oxygen and NO adsorbed on the BT-L surface to form NO₂⁻, NO₃⁻, etc., thereby achieving the effect of air purification.

4. Conclusion

In conclusion, the Bi₄Ti₃O₁₂ nanowires with abundant oxygen vacancies and grown along the [010] direction was successfully synthesized via a hydrothermal method with the addition of a structure-inducing agent. Bi₄Ti₃O₁₂ nanowires exhibited excellent photocatalytic NO removal performance, which is attributed to improved polarization and extended photosensitivity range. Theoretical

calculations support that the generation of oxygen vacancies and the oriented growth of Bi₄Ti₃O₁₂ improve the polarization intensity along [010] direction. Moreover, oxygen vacancy-modified Bi₄Ti₃O₁₂ exhibited increased polarization intensity primarily in the [010] direction, and the presence of oxygen vacancies gradually shift the dominant polarization direction of Bi₄Ti₃O₁₂ from [100] to [010]. The improved polarization and expanded light response range of Bi₄Ti₃O₁₂ give rise to its enhanced photocatalytic NO removal efficiency. This study provides a feasible strategy for enhancing ferroelectricity to improve photocatalytic performance and could be extended to other bismuth layer-structured ferroelectrics.

CRediT authorship contribution statement

Wang Junjun: Writing – review & editing, Visualization. **Wang Yu:** Writing – review & editing, Visualization. **Zhu Qiuhui:** Writing – original draft, Visualization, Validation, Methodology, Investigation, Conceptualization. **Xu Jingsan:** Writing – review & editing. **Luo Jian-min:** Writing – review & editing, Visualization. **Wang Chuanyi:** Writing – review & editing, Visualization, Supervision, Resources, Project administration, Conceptualization.

Declaration of Competing Interest

The authors declare that they have no known competing financial interests or personal relationships that could have appeared to influence the work reported in this paper.

Data availability

No data was used for the research described in the article.

Acknowledgments

This work was supported by the National Natural Science Foundation of China (Nos. 52161145409, 21976116), Shaanxi Science and Technology Program (2020KWZ-005), Foreign Expert Project of SAFEA of China (DL2023041004L and G2023041021L), and the Introduced Talent Start-up Fund Project of Wuyi University (Grant No. YJ202325).

Appendix A. Supporting information

Supplementary data associated with this article can be found in the online version at [doi:10.1016/j.apcatb.2024.123734](https://doi.org/10.1016/j.apcatb.2024.123734).

References

- [1] A. Mei, Z. Xu, X. Wang, Y. Liu, J. Chen, J. Fan, Q. Shi, Photocatalytic materials modified with carbon quantum dots for the degradation of organic pollutants under visible light: A review, *Environ. Res.* 9 (2022) 114160.
- [2] X. Zhang, Y. Liu, Q. Zhang, Y. Zhou, Bismuth and bismuth composite photocatalysts, *Prog. Chem.* 28 (2016) 1560–1568.
- [3] H. Kunioku, M. Higashi, O. Tomita, M. Yabuuchi, D. Kato, H. Fujito, H. Kageyama, R. Abe, Strong hybridization between Bi-6s and O-2p orbitals in Sillén–Aurivillius perovskite $\text{Bi}_4\text{MO}_8\text{X}$ ($\text{M} = \text{Nb}$, Ta ; $\text{X} = \text{Cl}$, Br), visible light photocatalysts enabling stable water oxidation, *J. Mater. Chem. A* 6 (2018) 3100–3107.
- [4] K. Inzani, N. Pokhrel, N. Leclerc, Z. Clemens, S.P. Ramkumar, S.M. Griffin, E. A. Nowadnick, Manipulation of spin orientation via ferroelectric switching in Fe-doped Bi_2WO_6 from first principles, *Phys. Rev. B* 105 (2022) 054434.
- [5] H. Sun, Z. Xu, X. Xie, H. Niu, M. Wang, X. Zhang, X. Chen, J. Han, Enhanced photocatalytic activity of ferroelectric-based $\text{Ag}_2\text{O}/\text{Bi}_4\text{Ti}_3\text{O}_{12}$ hybrids piezoelectric Eff. *J. Alloy. Compd.* 882 (2021) 160609.
- [6] A. Roy, R. Prasad, S. Auluck, A. Garg, First-principles calculations of Born effective charges and spontaneous polarization of ferroelectric bismuth titanate, *J. Phys.: Condens. Matter* 22 (2010) 165902.
- [7] S. Supriya, Tailoring layered structure of bismuth-based aurivillius perovskites: recent advances and future aspects, *Coord. Chem. Rev.* 479 (2023) 215010.
- [8] J. Dorrian, R. Newnham, D. Smith, M. Kay, Crystal structure of $\text{Bi}_4\text{Ti}_3\text{O}_{12}$, *Ferroelectrics* 3 (1972) 17–27.
- [9] X. Xie, Z. Zhou, B. Gao, Z. Zhou, R. Liang, X. Dong, Ion-pair engineering-induced high piezoelectricity in $\text{Bi}_4\text{Ti}_3\text{O}_{12}$ -based high-temperature piezoceramics, *ACS Appl. Mater. Interfaces* 14 (2022) 14321–14330.
- [10] K. Klyukin, V. Alexandrov, The effect of intrinsic point defects on ferroelectric polarization behavior of SrTiO_3 , *Phys. Rev. B* 95 (2016) 035301.
- [11] Q.H. Zhu, A.A. Dar, Y.T. Zhou, K. Zhang, J.N. Qin, B. Pan, J.Q. Lin, A.O. T. Patrocínio, C.Y. Wang, Oxygen vacancies promoted piezoelectricity toward piezo-photocatalytic decomposition of tetracycline over $\text{SrBi}_4\text{Ti}_4\text{O}_{15}$, *ACS EST Engg* 2 (2022) 1365–1375.
- [12] G. Sun, J. Kürti, P. Rajczy, M. Kertesz, J. Hafner, G. Kresse, Performance of the Vienna ab initio simulation package (VASP) in chemical applications, *J. Mol. Struct.: J. Mol. Struct.-Theorchem.* 624 (2003) 37–45.
- [13] J.P. Perdew, K. Burke, M. Ernzerhof, Perdew, burke, and ernzerhof reply, *Phys. Rev. Lett.* 80 (1998) 891.
- [14] M. Gajdoš, K. Hummer, G. Kresse, J. Furthmüller, F. Bechstedt, Linear optical properties in the projector-augmented wave methodology, *Phys. Rev. B* 73 (2006) 045112.
- [15] X. Du, I.W. Chen, Ferroelectric thin films of bismuth-containing layered perovskites: part I, $\text{Bi}_4\text{Ti}_3\text{O}_{12}$, *J. Am. Ceram. Soc.* 81 (1998) 3253–3259.
- [16] H.J. Liu, P. Chen, X.Y. Yuan, Y.X. Zhang, H.W. Huang, L. Wang, F. Dong, Pivotal roles of artificial oxygen vacancies in enhancing photocatalytic activity and selectivity on $\text{Bi}_2\text{O}_2\text{CO}_3$ nanosheets, *Chinese, J. Catal.* 40 (2019) 620–630.
- [17] J. Jiang, K. Zhao, X. Xiao, L. Zhang, Synthesis and facet-dependent photoreactivity of BiOCl single-crystalline nanosheets, *J. Am. Chem. Soc.* 134 (2012) 4473–4476.
- [18] X. Xiong, L. Ding, Q. Wang, Y. Li, Q. Jiang, J. Hu, Synthesis and photocatalytic activity of BiOBr nanosheets with tunable exposed {010} facets, *Appl. Catal. B-Environ.* 188 (2016) 283–291.
- [19] G. Wang, Q. Deng, H. Li, W. Hou, Mannitol and acidity co-tuned synthesis of oxygen-vacancy-modified bismuth molybdate nanorods for efficient photocatalytic nitrogen reduction to ammonia, *Sci. China Mater.* 66 (2023) 1435–1446.
- [20] W.K. Son, J.H. Youk, T.S. Lee, W.H. Park, Effect of pH on electrospinning of poly (vinyl alcohol), *Mater. Lett.* 59 (2005) 1571–1575.
- [21] A. Xu, X. Chen, D. Wei, B. Chu, M. Yu, X. Yin, J. Xu, Regulating the electronic structure of bismuth nanosheets by titanium doping to boost CO_2 electroreduction and $\text{Zn}-\text{CO}_2$ batteries, *Small* 19 (2023) 2302253.
- [22] Z. Luo, X. Ye, S. Zhang, S. Xue, C. Yang, Y. Hou, W. Xing, R. Yu, J. Sun, Z. Yu, Unveiling the charge transfer dynamics steered by built-in electric fields in BiOBr photocatalysts, *Nat. Commun.* 13 (2022) 2230.
- [23] Y. Liu, M. Zhang, Z. Wang, J. He, J. Zhang, S. Ye, X. Wang, D. Li, H. Yin, Q. Zhu, Bipolar charge collecting structure enables overall water splitting on ferroelectric photocatalysts, *Nat. Commun.* 13 (2022) 4245.
- [24] J. Ye, B. Zhu, B. Cheng, C. Jiang, S. Wageh, A.A. Al-Ghamdi, J. Yu, Synergy between platinum and gold nanoparticles in oxygen activation for enhanced room-temperature formaldehyde oxidation, *Adv. Funct. Mater.* 32 (2022) 2110423.
- [25] R. Hosseini, A. Fattah-alhosseini, M. Karbasi, S. Giannakis, Tailoring surface defects in plasma electrolytic oxidation (PEO) treated 2-D black TiO_2 : Post-treatment role, and intensification by peroxymonosulfate activation in visible light-driven photocatalysis, *Appl. Catal. B-Environ.* 340 (2024) 123197.
- [26] Q. Ren, Y. He, H. Wang, Y. Sun, F. Dong, Photo-switchable oxygen vacancy as the dynamic active site in the photocatalytic NO oxidation reaction, *ACS Catal.* 12 (2022) 14015–14025.
- [27] Y. Zhang, T. Song, X. Zhou, Y. Yang, Oxygen-vacancy-boosted visible light driven photocatalytic oxidative dehydrogenation of saturated N-heterocycles over Nb_2O_5 nanorods, *Appl. Catal. B-Environ.* 316 (2022) 121622.
- [28] Y. Dai, B. Liu, Z. Zhang, P. Guo, C. Liu, Y. Zhang, L. Zhao, Z. Wang, Tailoring the d-orbital splitting manner of single atomic sites for enhanced oxygen reduction, *Adv. Mater.* 35 (2023) 2210757.
- [29] Q. Tang, J. Wu, X.-Z. Chen, R. Sanchis-Gual, A. Veciana, C. Franco, D. Kim, I. Surin, J. Pérez-Ramírez, M. Mattera, Tuning oxygen vacancies in $\text{Bi}_4\text{Ti}_3\text{O}_{12}$ nanosheets to boost piezo-photocatalytic activity, *Nano Energy* 108 (2023) 108202.
- [30] W. Tu, Y. Xu, J. Wang, B. Zhang, T. Zhou, S. Yin, S. Wu, C. Li, Y. Huang, Y. Zhou, Investigating the role of tunable nitrogen vacancies in graphitic carbon nitride nanosheets for efficient visible-light-driven H_2 evolution and CO_2 reduction, *ACS Sustain. Chem. Eng.* 5 (2017) 7260–7268.
- [31] X. Wu, D. Li, B. Luo, B. Chen, Y. Huang, T. Yu, N. Shen, L. Li, W. Shi, Molecular-level insights on NIR-driven photocatalytic H_2 generation with ultrathin porous S-doped g- C_3N_4 nanosheets, *Appl. Catal. B-Environ.* 325 (2023) 122292.
- [32] H. Li, H. Zhu, Y. Shi, H. Shang, L. Zhang, J. Wang, Vacancy-rich and porous NiFe-layered double hydroxide ultrathin nanosheets for efficient photocatalytic NO oxidation and storage, *Environ. Sci. Technol.* 56 (2022) 1771–1779.
- [33] T. Xue, L. Chen, K. Li, B. Lei, H. Wang, F. Dong, Y. Yang, Highly enhanced photocatalytic NO removal and inhibited peroxyacetyl nitrate formation in synergistic acetaldehyde degradation, *Environ. Sci. Technol.* 57 (2023) 8174–8182.
- [34] Q. Zhu, R. Hailili, Y. Xin, Y. Zhou, Y. Huang, X. Pang, K. Zhang, P.K.J. Robertson, D.W. Bahnemann, C. Wang, Efficient full spectrum responsive photocatalytic NO conversion at $\text{Bi}_2\text{Ti}_2\text{O}_7$: Co-effect of plasmonic Bi and oxygen vacancy, *Appl. Catal. B-Environ.* 319 (2022) 121888.
- [35] P. Chen, H. Liu, Y. Sun, J. Li, W. Cui, La Wang, W. Zhang, X. Yuan, Z. Wang, Y. Zhang, F. Dong, Bi metal prevents the deactivation of oxygen vacancies in $\text{Bi}_2\text{O}_2\text{CO}_3$ for stable and efficient photocatalytic NO abatement, *Appl. Catal. B-Environ.* 264 (2020) 118545.
- [36] W. He, Y. Sun, G. Jiang, Y. Li, X. Zhang, Y. Zhang, Y. Zhou, F. Dong, Defective $\text{Bi}_4\text{MoO}_9/\text{Bi}$ metal core/shell heterostructure: enhanced visible light photocatalysis and reaction mechanism, *Appl. Catal. B-Environ.* 239 (2018) 619–627.
- [37] Y. Xin, Q. Zhu, T. Gao, X. Li, W. Zhang, H. Wang, D. Ji, Y. Huang, M. Padervand, F. Yu, C. Wang, Photocatalytic NO removal over defective Bi/ BiOBr nanoflowers: The inhibition of toxic NO_2 intermediate via high humidity, *Appl. Catal. B-Environ.* 324 (2023) 122238.
- [38] M. Gu, Y. Li, M. Zhang, X. Zhang, Y. Shen, Y. Liu, F. Dong, Bismuth nanoparticles and oxygen vacancies synergistically attired Zn_2SnO_4 with optimized visible-light-active performance, *Nano Energy* 80 (2021) 105415.
- [39] H. Wu, C. Yuan, R. Chen, J. Wang, F. Dong, J. Li, Y. Sun, Mechanisms of interfacial charge transfer and photocatalytic NO oxidation on $\text{BiOBr}/\text{SnO}_2$ p-n Heterojunctions, *ACS Appl. Mater. Interfaces* 12 (2020) 43741–43749.